AI for Materials
https://www.sciltp.com/journals/AIMat

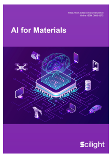

Review

Advances in Machine Learning Potentials for Mineral Physics at High Pressure and High Temperature

Lei Wan [1,2] and Yunguo Li [1,2,*]

[1] State Key Laboratory of Lithospheric and Environmental Coevolution, School of Earth and Space Sciences, University of Science and Technology of China, Hefei 230026, China
[2] Deep Space Exploration Laboratory, Hefei 230026, China
* Correspondence: liyunguo@ustc.edu.cn

How To Cite: Wan, L.; Li, Y. Advances in Machine Learning Potentials for Mineral Physics at High Pressure and High Temperature. *AI for Materials* **2026**, *1*(1), 7. https://doi.org/10.53941/aimat.2026.100007

Received: 6 November 2025
Revised: 17 January 2026
Accepted: 26 January 2026
Published: 2 February 2026

Abstract: Understanding the composition and physical properties of Earth's deep interior is fundamental to deciphering planetary evolution, yet modeling these systems under extreme pressure–temperature (P–T) conditions remains a significant challenge. While first-principles simulations based on density functional theory (DFT) offer high accuracy, their prohibitive computational costs typically restrict studies to small scales and short timescales. Recently, machine learning potentials (MLPs) have emerged as a transformative bridge, providing near-first-principles fidelity at a fraction of the cost and enabling large-scale simulations of complex materials under deep-Earth conditions. This review synthesizes recent progress in applying MLPs to high P–T mineral physics, focusing on breakthroughs in modeling thermodynamic, transport, and elastic properties. We discuss methodological hurdles in extending MLPs across broad P–T ranges and evaluate emerging strategies—such as active learning, uncertainty quantification and temperature-dependent training—to overcome them. By uncovering phenomena like superionic conduction and defect-controlled behavior, MLPs are shifting our perspective of the deep Earth from idealized models toward complex, dynamic systems, paving the way for a predictive, data-driven era in mineral physics.

Keywords: machine learning potential; high pressure high temperature; transport properties; seismic properties; thermodynamic properties

1. Introduction

The Earth's deep interior, particularly the mantle and core, plays a pivotal role in understanding our planet's origin, evolution, and internal dynamics through the study of its composition and physical properties. However, natural samples are only available to the depth up to the bottom of transition zone [1,2]. The study of the most part of Earth's interior has to rely on the experimental and theoretical modeling. As shown in Figure 1, the lower mantle experiences pressures ranging from approximately 24 GPa at the base of the transition zone to about 136 GPa near the core-mantle boundary, while temperatures increase from around 1839 K to roughly 4100 K [3–5]. Conditions in the core are even more extreme, with pressures reaching up to 360 GPa in the center and temperatures likely exceeding 5400 K at the inner core boundary [6]. The structures and properties of materials under such conditions are in stark contrast to those under ambient conditions.

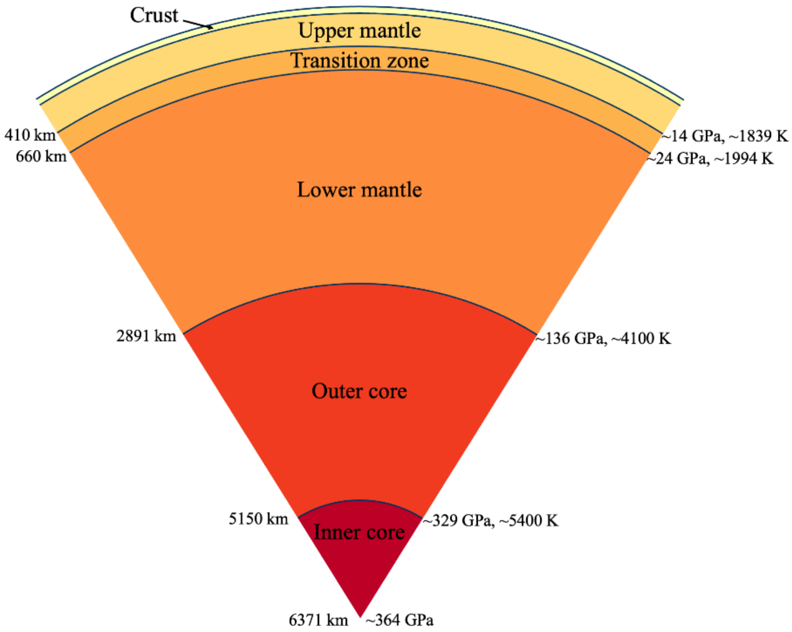

Figure 1. Schematic diagram of the pressure-temperature conditions in Earth's interior. Pressure data are from Ref. [3]. Temperature data for the transition zone are from Ref. [5]. Temperature at the core–mantle boundary is from Ref. [4]. Temperature data at the inner–outer core boundary is from Ref. [6].

Experimental investigations of Earth's deep interior remain inherently challenging because of the extreme pressures and temperatures characteristic of these regions [7]. High P–T experiments are indispensable tools for probing the physical properties of deep-Earth materials, as they enable researchers to reproduce relevant thermodynamic conditions in the laboratory. However, such experiments face several intrinsic limitations. Constrained by instrumentation, the accessible sample volumes are typically small, producing weak signals that require exceptionally sensitive detection systems [8,9]. Moreover, pronounced pressure and temperature gradients within the sample chamber can introduce significant uncertainties in the derived data [8]. In many cases, in situ observations are not feasible, and samples must be quenched to ambient conditions for ex situ analyses—an approach that may alter their structures and phase relations, leading to deviations from the true high P–T states [10,11]. These challenges collectively limit the precision and reproducibility of experimental constraints on the properties and behaviors of materials in Earth's deep interior.

Theoretical and computational methods provide an essential complement to experiments in exploring the properties of Earth's deep materials. Among them, first-principles calculations based on DFT have become a cornerstone of mineral physics owing to their predictive accuracy and parameter-free nature [12,13]. By explicitly solving the electronic structure, DFT enables the computation of interatomic forces and total energies with high fidelity, offering reliable predictions across a broad range of P–T conditions relevant to the entire Earth's interior. Such calculations have been instrumental in determining equations of state [14,15], thermodynamic and elastic properties [16–21], and various transport properties [22–25] of deep-Earth materials.

Despite these advantages, first-principles simulations are constrained by their substantial computational cost, which limits accessible system sizes and timescales. Typical simulations involve only a few hundred atoms and extend over picosecond to nanosecond durations—insufficient for capturing large-scale structural heterogeneity or slow dynamic processes [26,27]. At lower temperatures, where atomic mobility decreases, achieving chemical or structural equilibrium requires longer sampling times to adequately explore the phase space, further compounding computational demands. These constraints hinder the direct application of DFT to complex, multicomponent systems under realistic mantle and core conditions.

In recent years, MLPs have emerged as an efficient and accurate alternative for modeling materials under extreme conditions [28,29]. They bridge the long-standing gap between the high accuracy but prohibitive cost of first-principles methods and the computational efficiency but limited transferability of empirical potentials. Trained on datasets generated from first-principles calculations, MLPs can reproduce interatomic forces and energies with near first-principles accuracy while reducing computational cost by several orders of magnitude [27,30,31]. This capability enables simulations involving tens of thousands of atoms over nanosecond-to-microsecond timescales—conditions that are far closer to those within Earth's deep interior than previously attainable.

MLPs have already been widely applied in studies of deep-Earth materials, yielding significant advances under mantle and core P–T regimes. For instance, MLP-based simulations have been used to investigate the thermal conductivity of bridgmanite and post-perovskite in the lower mantle, refining estimates of heat flux across the core–mantle boundary and thereby improving our understanding of the thermal budget and magnetic field evolution of the planet [32]. Deep-learning molecular dynamics has also enabled large-scale simulations of iron at core conditions, employing supercells to determine the densities and equations of state of the hexagonal close-packed (hcp) and body-centered cubic (bcc) phases [33,34]. In addition, MLPs have been applied to study the partitioning and behavior of light elements in the core [35,36]. Such simulations reveal how elements like sulfur, oxygen, and hydrogen influence core density, elasticity, and thermodynamic properties, offering new insights into the formation and evolution of Earth's core.

Consequently, this review summarizes recent progress in applying MLPs to mineral physics, specifically under extreme high-pressure and high-temperature conditions. We explore how MLPs elucidate the composition, transport properties, elastic behavior, and thermodynamics of Earth's deep materials. Furthermore, we discuss current challenges and emerging strategies for extending MLPs toward more realistic, chemically complex, and defect-bearing systems. For a broader discussion on the developmental roadmap of MLPs, readers are referred to several other recent reviews [37,38].

2. Developing Machine Learning Potentials for Extreme Conditions

The central principle of a MLP is to approximate the interatomic potential energy surface (PES) based on reference data from first-principles calculations. In doing so, MLPs enable simulations of substantially larger atomic systems and longer timescales at a fraction of the computational cost, while maintaining accuracy comparable to quantum mechanical methods.

Current approaches to constructing MLPs can be broadly divided into two categories: descriptor-based models and message-passing models. Descriptor-based models—such as neural network potentials (NNPs), Gaussian approximation potentials (GAPs), and moment tensor potentials (MTPs)—encode each atom's local environment into mathematical descriptors, which are then used by regression algorithms (e.g., neural networks or Gaussian processes) to fit the first-principles PES [27,39]. In contrast, message-passing neural networks (MPNNs), such as PhysNet [40], represent atomic systems as graphs, learning interatomic interactions through iterative message exchanges between nodes. These frameworks have significantly improved the efficiency and generalization of MLPs across complex chemical and structural spaces.

2.1. Workflow for Developing MLPs

The typical workflow for developing a MLP involves four key stages (Figure 2):

(1) Dataset generation. A diverse training dataset is constructed using first-principles calculations that provide atomic structures, total energies, forces, and stresses.
(2) MLP training. A machine learning potential is trained to map atomic configurations to corresponding energies and forces.
(3) MLP validation. The trained potential is evaluated against an independent validation set to assess accuracy and transferability.
(4) Application. The validated MLP is then employed in large-scale molecular dynamics (MD) simulations or structure searches to explore materials behavior under target conditions.

The quality and diversity of the training dataset critically determine the reliability of the resulting potential. To capture relevant regions of configurational space, the dataset must include a broad variety of atomic arrangements representative of the target P–T conditions. Constructing such datasets typically involves extensive first-principles molecular dynamics simulations followed by strategic sampling.

Figure 2 presents the overall workflow for training MLPs from first-principles data using active learning. The iterative scheme starts by training one or more initial MLP on a small seed dataset, then uses these MLPs to perform molecular dynamics simulations. Configurations for which the MLPs yield unreliable predictions are identified from the MD results as candidate structures. These candidates are recomputed with first-principles methods and appended to the training set. This iterative scheme begins with a small initial dataset to train a preliminary model, which is then used to perform MD or structure searches. When the model encounters configurations with high prediction uncertainty or extrapolation risk, those configurations are recomputed using first-principles methods and added to the training set. The potential is then retrained, and the cycle repeats until convergence. Active learning thus minimizes redundant first-principles calculations, systematically explores the configuration space, and enhances both training efficiency and model robustness. Active learning has emerged as an efficient strategy to optimize dataset construction (Figure 2) [41,42].

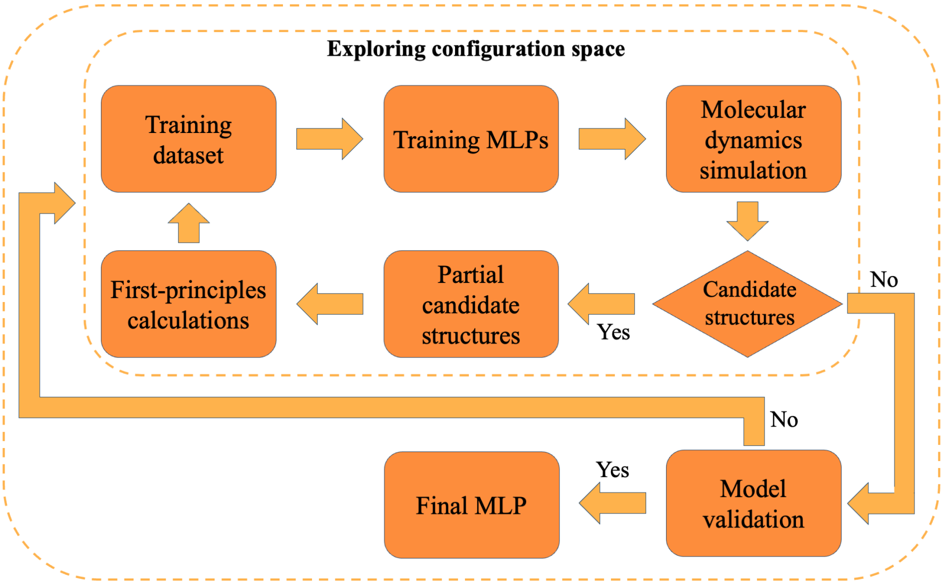

Figure 2. Schematic diagram of the machine learning potential training workflow.

Because MLPs are data-driven, the quality of the first-principles reference data is paramount. Variations in exchange–correlation functionals, plane-wave cutoff energies, *k*-point sampling, or pseudopotentials can lead to systematic deviations in the fitted potential. Therefore, careful convergence testing of all first-principles parameters is essential before dataset generation and model fitting.

2.2. Toward Universal and Transferable Potentials

Beyond system-specific models, recent studies have focused on developing general-purpose or universal MLPs capable of spanning broader chemical and structural spaces. Examples include MatterGen, CHGNet, and M3GNet [43–45]. These models incorporate multimodal training data—energies, forces, and stresses—and leverage message-passing architectures to achieve high accuracy in predicting thermodynamic stability, structural relaxation, and materials properties. Their transferability has accelerated materials discovery and enabled cross-scale simulations such as crystal structure prediction, defect energetics, and alloy design [46].

However, the reliability of universal potentials strongly depends on the quality, diversity, and representativeness of their training datasets. Expanding chemical and P–T coverage requires vastly larger and more varied configuration spaces, which in turn demands significant computational resources. Consequently, universal MLPs often show somewhat larger errors in energy and force predictions than specialized models optimized for a single system. Achieving an optimal balance between generality and accuracy—while maintaining manageable computational cost—remains a central challenge. Moreover, obtaining high-precision thermodynamic properties, such as free energies and melting points, places particularly stringent demands on MLP accuracy, an area where current universal models still require improvement.

2.3. Challenges under Extreme Pressure–Temperature Conditions

At present, no universal MLP has been published that fully covers the extreme P–T conditions of Earth's interior, as the relevant configurational space expands dramatically with increasing P and T. Elevated pressures compress atomic volumes, shorten bond lengths, and drive complex phase transitions. They can also induce charge redistribution, causing transitions from semiconducting to metallic [47], or even metallic to insulating [48], states. In some cases, electrons localize at interstitial sites to form electrides [49]. These effects pose additional challenges for potential fitting compared with ambient conditions.

Temperature introduces another layer of complexity through the contribution of electronic entropy, which varies significantly at high temperature. As shown in Figure 3, the electronic-entropy contribution to the total energy increases sharply with temperature even for the same atomic configuration. Standard MLPs, which do not explicitly account for electronic temperature, yield identical energies across temperatures, neglecting this important effect.

Two main strategies have been proposed to incorporate temperature dependency of electronic properties:

1. Multiple-temperature training, in which separate MLPs are trained on datasets generated at different electronic temperatures to span a wide P–T range [33].
2. Explicit electronic temperature dependent MLPs, where the electronic temperature term is embedded directly into the model architecture [50].

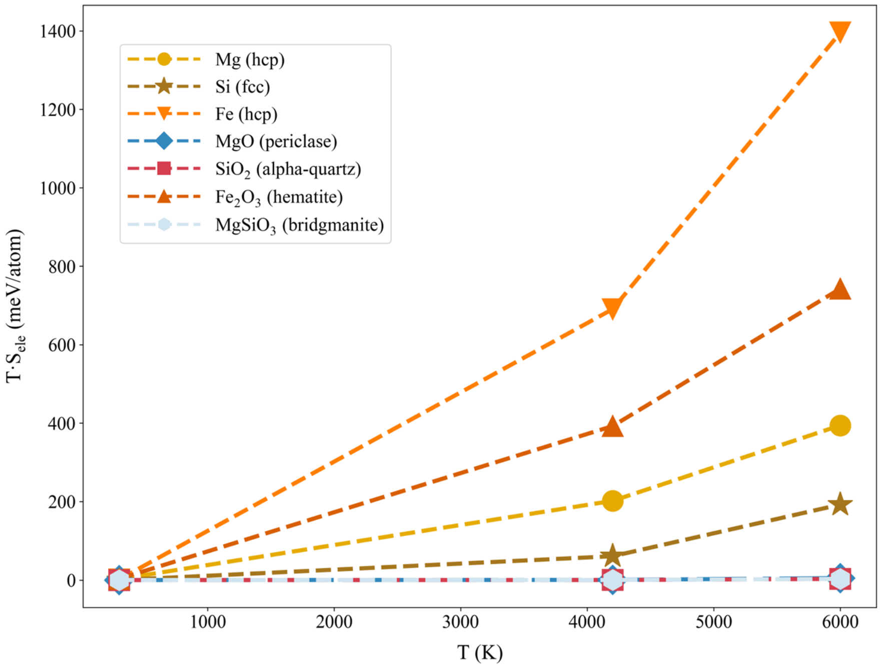

Figure 3. The contribution of electronic entropy of different materials to the energy of the system changes with the electronic temperature (300 K, 4200 K, 6000 K) at 0 GPa. Static calculations were performed for each material at varying electronic temperature.

For many systems near ambient conditions, the electronic-entropy contribution to total energy is small and varies little with temperature, so the temperature dependence of electronic entropy is often neglected during the training of many MLPs. However, under the thousands of Kelvin and hundreds of gigapascal conditions characteristic of Earth's deep interior (Figure 2), this contribution becomes substantial and must be explicitly included during training. The divergent melting point predictions for iron reported by Yuan and Steinle-Neumann (2023) [51] and Wu et al. (2024) [52] highlight the importance of incorporating electronic-entropy effects in MLPs designed for extreme high P–T simulations. A practical guideline is to implement electronic-temperature corrections whenever the variation in the electronic-entropy energy term exceeds the target accuracy threshold of the potential.

3. Applications of Machine Learning Potentials under Extreme Conditions

MLPs have been increasingly employed to investigate a broad range of physical and chemical processes in Earth's deep interior. By enabling large-scale, long-timescale simulations with near–first-principles accuracy, MLPs allow quantitative exploration of transport, mechanical, and thermodynamic properties under realistic P–T conditions. These studies reveal the critical role of composition, volatile content, and structural defects in governing deep-Earth dynamics.

3.1. Transport Properties

Transport processes—including the transfer of heat, mass, and charge—control Earth's thermal evolution, compositional differentiation, and magnetic field generation. Key parameters such as thermal conductivity, electrical conductivity, viscosity, and diffusion coefficients determine mantle convection, melt dynamics, and the cooling rate of the core. These quantities normally need long-time MD simulations and are hard to converge, so the calculations with heavy DFT methods usually come with large uncertainties [13,53]. MLP-based molecular dynamics (MLP-MD) simulations have become essential tools for quantifying these transport properties and their dependencies on temperature, pressure, and composition.

3.1.1. Thermal Conductivity

Thermal conductivity critically influences the cooling rate of the magma ocean, the heat flux across the core–mantle boundary (CMB), and the thermal structure of subducting slabs. Experimental determinations of thermal conductivity under high P–T conditions remain challenging, and reported values often vary substantially [54–57]. Although first-principles and non-equilibrium molecular dynamics (NEMD) simulations provide valuable insights, their small cell sizes introduce significant size effects. MLPs, which combine first-principles accuracy with large-scale simulation capability, have overcome this limitation and yielded new quantitative constraints on mineral and melt conductivities.

MLP-based studies have explored the effects of temperature, pressure, water, and iron content on the thermal conductivity of minerals in the mantle transition zone (MTZ) and lower mantle. Because the MTZ is likely to be water-rich [1,58], its conductivities are expected to be significantly altered by hydration. In wadsleyite, MLP–NEMD simulations show that 0.81 wt% and 1.63 wt% H_2O reduce lattice thermal conductivity by ~10% and ~12%, respectively, and also diminish anisotropy [59]. Water in olivine and ringwoodite exerts similar effects [60,61].

For $MgSiO_3$ melt, the thermal conductivity at CMB conditions is ~4.0 W m^{-1} K^{-1}—significantly lower than that of the solid mantle—potentially explaining lateral CMB heat-flux variations and the formation of ultra-low velocity zones (ULVZs) [62–64]. Pressure dominates the conductivity trend, while temperature and water exert weaker influence. In the lower mantle, the bridgmanite–post-perovskite transition increases the thermal conductivity of pyrolite by ~22% [32]. The addition of 12.5 mol% Fe reduces the thermal conductivities of bridgmanite and post-perovskite by ~10% and ~14% [32], respectively, and water further decreases thermal conductivity and weakens thermal anisotropy [63]. Collectively, these effects revealed by using MLPs suggest that hydration may reduce lateral heterogeneity in CMB heat flux.

3.1.2. Electrical Conductivity

Experimental measurements of silicate melt electrical conductivity over the entire mantle range are scarce, and conventional first-principles simulations are restricted to high temperatures due to slow atomic diffusion. MLPs enable extensive simulations across wide P–T conditions, elucidating pressure and compositional dependencies.

For $MgSiO_3$ melt, MLPs studies reveal that its electrical conductivity increases with temperature but exhibits a nonmonotonic pressure dependence, peaking near 50 GPa (~420 S/m) before decreasing toward the CMB (~26 S/m) along mantle liquidus [65]. This behavior may explain the sharp increase in mantle electrical conductivity inferred from geophysical observations. In bridgmanite and post-perovskite, hydrogen incorporation via $(Mg + 2H)_{Si}$ and $(Al + H)_{Si}$ substitution mechanisms was found to enhance proton conduction to levels consistent with mantle conductivity estimates [66], implying that lower mantle electrical conductivity could serve as a proxy for its water distribution. Moreover, superionic conduction has been identified in hydrous stishovite: at 30 GPa and 2500 K, hydrogen becomes mobile along one-dimensional channels, yielding anisotropic ionic conductivities up to 27 S/m [67].

3.1.3. Viscosity

Viscosity controls the dynamics of the early magma ocean, magma mobility, and core–mantle differentiation. Experimental measurements under high pressure often yield inconsistent trends [68–73]. MLP simulations reveal that for $MgSiO_3$ melt, viscosity decreases with increasing temperature and exhibits pressure-dependent behavior: at 2200 K it decreases then increases beyond ~6 GPa, while at 5000 K it increases monotonically. Along the mantle liquidus, a turnover near 23 GPa may correspond to melt accumulation near the 660 km discontinuity [65].

For hcp-Fe, MLP-based simulations attribute its relatively low viscosity (~$10^{15 \pm 1}$ Pa·s) to the high mobility of Fe atoms and the presence of vacancies [34], consistent with constraints from Earth's nutation and geodynamic models. This finding emphasizes the influence of structural defects and reduces the need for invoking excessive light element contents to explain core dynamics.

3.1.4. Diffusion

Elemental diffusion affects mantle mixing, water transport, and core–mantle exchange. MLP simulations allow accurate diffusion calculations for melts, crystals, and grain boundaries—previously inaccessible to small DFT-based cells.

In $MgSiO_3$ melt, MLPs simulations found that all atomic species exhibit decreasing diffusion coefficients with increasing pressure (>3000 K); Mg diffuses fastest, while the pressure dependence of Si and O diffusion mirrors the viscosity trend [65]. In bridgmanite and post-perovskite, hydrogen diffusion depends strongly on incorporation mechanisms: $(Mg + 2H)_{Si}$ and $(Al + H)_{Si}$ defects yield the highest diffusion rates, with diffusion faster in post-perovskite and anisotropic along [100] [66]. Slow H diffusion implies long-term heterogeneity in lower mantle hydration. In δ-AlOOH, hydrogen diffusion approaches ~1 $Å^2$/ns between 1800–2100 K, consistent with the onset of a fully superionic state [74].

MLPs also enable grain boundary diffusion simulations. Peng et al. (2025) found that W diffuses extremely slowly in ferropericlase and silicate melts at CMB conditions, with a maximum diffusion distance of ~30 m over Earth's age—far less than extrapolations from low-T experiments—indicating that W isotope anomalies in ocean island basalts cannot arise from grain boundary diffusion alone [75].

In summary, MLPs have revolutionized the quantitative study of transport properties, revealing that volatiles such as H_2O markedly reduce thermal conductivity and viscosity while enhancing ionic conductivity and diffusion. These effects collectively influence mantle convection, magnetic field generation, and the chemical evolution of Earth's deep interior.

3.2. Seismic Properties

Elasticity and seismic wave velocities provide fundamental constraints on the composition and structure of Earth's interior. MLPs enable atomistic modeling of elasticity, anisotropy, and defect effects at core and mantle conditions.

MLP simulations of hcp-Fe show an elastic anisotropy of ~6%, consistent with observed inner core anisotropy [34]. Polycrystalline averaging reduces shear wave velocity by up to 17%, improving agreement with seismic data. At inner core pressures, Fe–Si alloys exhibit a stable bcc phase stabilized by short-range Si ordering, matching PREM shear velocities better than hcp, fcc, or B2 structures [76].

In the core–mantle boundary region, superionic fcc-FeH exhibits V_p and V_s values ~34% and 63% lower than PREM, respectively, and a density 4% lower than the outer core but 50% higher than the lowermost mantle [77]. Mixtures of fcc-FeH with ambient mantle materials can reproduce the seismic characteristics of ULVZs, linking them to deep water cycling and hydrogen storage.

For $CaSiO_3$ perovskite, MLP studies reveal anomalous temperature-dependent elasticity: linear at high T but with pronounced precursor softening near the tetragonal–cubic transition [78]. The softening range widens with pressure and overlaps with cold slab geotherms, suggesting that subducted crustal materials with partially softened $CaSiO_3$ may explain the low shear velocities of large low shear velocity provinces (LLSVPs).

These studies suggest that MLPs provide critical insight into how intrinsic crystal anisotropy, structural defects, and phase transitions collectively shape seismic signatures throughout Earth's interior.

3.3. Thermodynamic Properties

Thermodynamic quantities—including melting points, phase stabilities, and element partitioning—are key to reconstructing Earth's thermal and chemical evolution. Combining MLPs with free energy and coexistence methods enables accurate thermodynamic predictions beyond the reach of direct DFT simulations.

3.3.1. Melting Behavior

MLPs have effectively removed size limitations in melting point calculations and have recently been widely used to compute melting temperatures of minerals in Earth's interior. Bridgmanite and post-perovskite are two major lower mantle mineral phases. Figure 4 compiles phase boundaries for bridgmanite, post-perovskite, and silicate melt determined previously by experiments and calculations. Dashed lines and open symbols represent earlier reports of bridgmanite melting points [79–88]. Red and blue solid symbols denote results obtained by starting from $MgSiO_3$ in experiments, raising temperature and pressure to the target conditions, and identifying the resulting mineral structures. These data were further used to determine the phase boundary between bridgmanite and post-perovskite [89,90]. The orange curve shows the MLP-based results of Deng et al. (2023) [42]. Their findings are consistent with prior determinations of both the bridgmanite melting curve and the phase boundary between bridgmanite and post-perovskite, indicating the accuracy of MLP calculations for melting. MLP calculations predict a melting temperature for periclase at 140 GPa of 7750 ± 50 K [64]. Moreover, MLPs have been applied to study superionic transitions in lower mantle minerals. $CaSiO_3$ perovskite containing oxygen vacancies undergoes superionic transition driven by oxygen's diffusion, with higher vacancy concentrations expanding the superionic region and lowering the transition temperature [91].

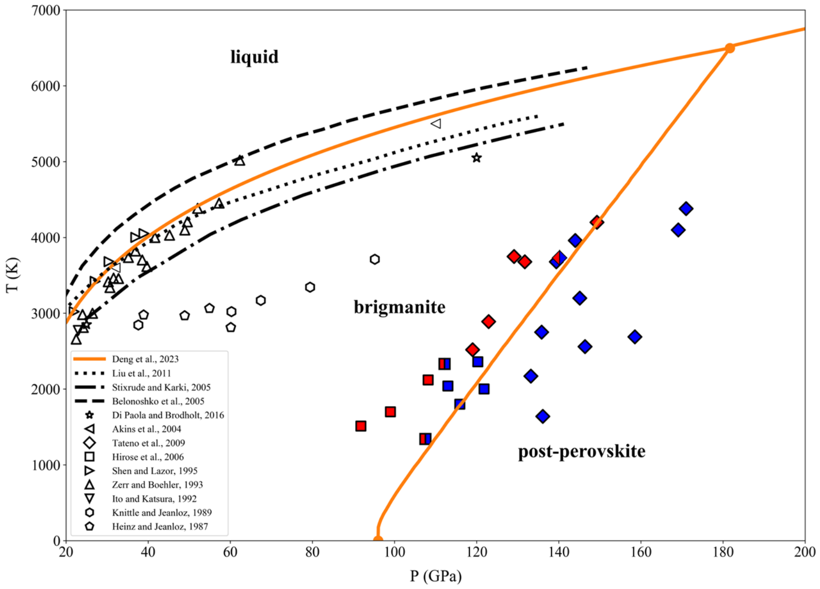

Figure 4. Melting of bridgmanite and post-perovskite. The orange solid line in the figure represents the melting curves of bridgmanite and post-perovskite, as well as the phase boundary between them, calculated using MLPs by Deng et al. (2023) [42]. The three dashed lines and open symbols indicate previously reported melting points of bridgmanite [79–88]. Solid red symbols represent experimental runs where only bridgmanite crystals were present. Solid blue symbols denote runs containing only post-perovskite crystals. Red-blue symbols correspond to experimental products where both bridgmanite and post-perovskite coexist [89,90].

For the core, MLPs simulations found that fcc-FeH melts near 2950 K at 130 GPa, while $FeH_{0.5}$ and $FeH_{0.25}$ melt at ~3250 K and 3630 K, respectively [77], implying stability of superionic FeH_x phases at the CMB. At the pressure of Earth's inner core boundary, discrepancies among studies emphasize the need for electronic-entropy corrections. Yuan and Steinle-Neumann (2023) [51] obtained a melting point of 7000–7100 K for hcp-Fe, reduced by 700–900 K with 0.34 wt% H, whereas Wu et al. (2024) [52] using an electronic temperature dependent Deep Potential (Tel-DP) found 6370 ± 200 K for hcp-Fe—resolving prior discrepancies and underscoring the importance of accurate electronic free-energy treatment.

3.3.2. Phases and Structures

MLPs have clarified several long-standing uncertainties in phase stability. Simulations show that MgO exsolves from liquid Fe in a crystalline ferropericlase form, providing a plausible but limited energy source for the early geodynamo [64]. For $CaSiO_3$ perovskite, MLPs were used to confirm a stable cubic phase throughout the lower mantle, with a tetragonal–cubic transition slope of ~7 K/GPa [92]. Oxygen vacancies promote a superionic phase that may contribute to mantle oxidation and deep oxygen cycling [91]. In hydrous stishovite, hydrogen atoms form one-dimensional channels and exhibit fluid-like motion upon heating, indicating partial superionic behavior [67].

3.3.3. Element Partitioning and Isotopic Fractionation

MLPs have enabled atomistic modeling of element partitioning and isotope fractionation, fundamental to understanding differentiation and volatile cycling. Simulations of metal–silicate equilibration reproduce experimental partitioning of light elements [93]. For the Fe–S system, the S partition coefficient increases with pressure up to ~250 GPa and then saturates near 0.75 [35], insufficient alone to explain the core's density deficit. In the Fe–H–O system, hydrogen preferentially resides in the liquid phase, but the presence of oxygen drives H incorporation into the solid core, reversing partitioning behavior when $O \geq 7$ mol% [36]. The inferred outer core may contain ~13.5 mol% H and 2.3–10.7 mol% O emphasizes non-ideal mixing among light elements.

Isotopic diffusion fractionation has also been explored via MLP-based pseudo-isotope simulations. In albite melts, the lithium isotope fractionation factor β decreases from 0.267 at 4000 K to 0.225 at 1800 K, with water slightly damping this temperature dependence. In model basaltic melts, β declines from 0.215 to 0.132 [94]. Similarly, β for helium in albite melt decreases from 0.355 at 3000 K to 0.322 at 1700 K, while in model basaltic melts, it decreases from 0.322 to 0.274 over the same temperature range [95], yielding $D(^3He)/D(^4He)$ ratios of 1.097 and 1.082, respectively—values consistent with natural observations.

As can be seen, MLPs enable precise evaluation of free energies, phase stability, and partitioning under extreme P–T conditions. They reveal widespread superionic and metastable states, strong coupling among light elements, and non-ideal mixing behavior—key to understanding chemical diversity, deep volatile cycling, and the dynamic evolution of Earth's interior.

4. Summary and Outlook

This review has systematically summarized recent advances in applying MLPs to mineral physics under the extreme P–T conditions of Earth's deep interior. Across three key domains—transport properties, mechanical behavior, and thermodynamic characteristics—MLPs have demonstrated their power to overcome the limitations of both laboratory experiments and first-principles calculations, advancing our ability to model complex processes that govern planetary evolution and dynamics.

Fundamentally, MLPs integrate the accuracy of quantum-mechanical methods with the efficiency of classical molecular dynamics, enabling large-scale simulations of tens of thousands of atoms over nanosecond and longer timescales at a fraction of the computational cost. This capability allows for direct, atomistic calculations of macroscopic properties such as thermal conductivity, viscosity, and diffusion, as well as quantitative evaluation of free energies, melting points, and phase equilibria. The application of MLPs has resolved long-standing discrepancies in predicted melting curves, seismic velocities, and transport coefficients, while unveiling new physical phenomena—such as superionic conduction, defect-governed transport, and strong coupling among light elements—that reshape our understanding of deep-Earth materials. These insights collectively depict a more dynamic and chemically heterogeneous interior than previously envisioned.

Despite these achievements, several challenges remain. The reliability of a MLP is intrinsically tied to the quality and diversity of its first-principles training data. Inconsistencies arising from the choice of exchange–correlation functional, *k*-point sampling, or pseudopotential can propagate into systematic errors. Insufficient sampling of configurational space can limit a potential's transferability beyond the conditions it was trained on. Furthermore, most existing MLPs are system-specific, making them difficult to generalize across compositions, phases, or pressure–temperature ranges.

Looking ahead, further efforts could focus more on several key directions.:

1. Developing transferable and temperature-dependent potentials that explicitly incorporate electronic entropy and maintain accuracy across wide P–T regimes.
2. Establishing standardized benchmarks and reporting protocols for training data, validation metrics, and uncertainty quantification to ensure reproducibility and comparability across studies.
3. Expanding training datasets through active learning and collaborative open repositories covering representative high P–T configurations of deep-Earth materials.
4. Integrating MLPs with multiscale modeling frameworks, linking atomic-scale processes to continuum models of mantle convection, core crystallization, and planetary evolution.

As machine learning techniques continue to evolve, the synergy between data-driven potentials, first-principles theory, and experimentation promises to transform mineral physics into a more predictive and integrative discipline. Ultimately, MLPs will not only deepen our understanding of Earth's interior but also illuminate the physics of planetary materials across the Solar System and beyond.

Author Contributions

L.W.: conceptualization, methodology, software, writing—original draft preparation, visualization, investigation; Y.L.: supervision, validation, writing—reviewing and editing. Both authors have read and agreed to the published version of the manuscript.

Funding

This research was funded by National Natural Science Foundation of China (No. 42322201) and CAS Hundred Talents Program.

Institutional Review Board Statement

Not applicable.

Informed Consent Statement

Not applicable.

Data Availability Statement

No new data were generated in this study.

Acknowledgments

The numerical calculations in this paper have been done on the supercomputing system in the Supercomputing Center of University of Science and Technology of China and in the Hefei Advanced Computing Center.

Conflicts of Interest

The authors declare no conflict of interest.

Use of AI and AI-Assisted Technologies

No AI tools were utilized for this paper.

References

1. Pearson, D.G.; Brenker, F.E.; Nestola, F.; et al. Hydrous mantle transition zone indicated by ringwoodite included within diamond. *Nature* **2014**, *507*, 221–224. https://doi.org/10.1038/nature13080.
2. Gu, T.T.; Pamato, M.G.; Novella, D.; et al. Hydrous peridotitic fragments of Earth's mantle 660 km discontinuity sampled by a diamond. *Nat. Geosci.* **2022**, *15*, 950–954. https://doi.org/10.1038/s41561-022-01024-y.
3. Dziewonski, A.M.; Anderson, D.L. Preliminary Reference Earth Model. *Phys. Earth Planet. Inter.* **1981**, *25*, 297–356. https://doi.org/10.1016/0031-9201(81)90046-7.
4. Stixrude, L.; de Koker, N.; Sun, N.; et al. Thermodynamics of silicate liquids in the deep Earth. *Earth Planet. Sci. Lett.* **2009**, *278*, 226–232. https://doi.org/10.1016/j.epsl.2008.12.006.
5. Katsura, T. A Revised Adiabatic Temperature Profile for the Mantle. *J. Geophys. Res. Solid Earth* **2022**, *127*, e2021JB023562. https://doi.org/10.1029/2021JB023562.
6. Alfè, D.; Gillan, M.J.; Price, G.D. Temperature and composition of the Earth's core. *Contemp. Phys.* **2007**, *48*, 63–80. https://doi.org/10.1080/00107510701529653.
7. Yamazaki, D.; Ito, E.; Yoshino, T.; et al. Over 1 Mbar generation in the Kawai-type multianvil apparatus and its application to compression of $(Mg_{0.92}Fe_{0.08})SiO_3$ perovskite and stishovite. *Phys. Earth Planet. Inter.* **2014**, *228*, 262–267. https://doi.org/10.1016/j.pepi.2014.01.013.
8. Irifune, T. Review Series to Celebrate Our 100th Volume Kawai-type multianvil ultrahigh-pressure technology. *Proc. Jpn. Acad. Ser. B Phys. Biol. Sci.* **2024**, *100*, 149–164. https://doi.org/10.2183/pjab.100.013.
9. Ishii, T.; Liu, Z.D.; Katsura, T. A Breakthrough in Pressure Generation by a Kawai-Type Multi-Anvil Apparatus with Tungsten Carbide Anvils. *Engineering* **2019**, *5*, 434–440. https://doi.org/10.1016/j.eng.2019.01.013.
10. Bondar, D.; Fei, H.Z.; Withers, A.C.; et al. A rapid-quench technique for multi-anvil high-pressure-temperature experiments. *Rev. Sci. Instrum.* **2020**, *91*, 065105. https://doi.org/10.1063/5.0005936.
11. Gion, A.M.; Gaillard, F.; Freslon, N.; et al. A method for the direct analysis of quenched, magmatic-hydrothermal fluids recovered from high-pressure, high-temperature experiments. *Chem. Geol.* **2022**, *609*, 121061. https://doi.org/10.1016/j.chemgeo.2022.121061.
12. Gillan, M.J.; Alfè, D.; Brodholt, J.; et al. First-principles modelling of Earth and planetary materials at high pressures and temperatures. *Rep. Prog. Phys.* **2006**, *69*, 2365–2441. https://doi.org/10.1088/0034-4885/69/8/R03.
13. Alfè, D.; Gillan, M.J. First-principles calculation of transport coefficients. *Phys. Rev. Lett.* **1998**, *81*, 5161–5164. https://doi.org/10.1103/PhysRevLett.81.5161.
14. Oganov, A.R.; Brodholt, J.P.; Price, G.D. Ab initio elasticity and thermal equation of state of $MgSiO_3$ perovskite. *Earth Planet. Sci. Lett.* **2001**, *184*, 555–560. https://doi.org/10.1016/S0012-821x(00)00363-0.
15. Sun, T.; Brodholt, J.P.; Li, Y.G.; et al. Melting properties from free energy calculations: Iron at the Earth's inner-core boundary. *Phys. Rev. B* **2018**, *98*, 224301. https://doi.org/10.1103/PhysRevB.98.224301.
16. Li, Y.G.; Vočadlo, L.; Sun, T.; et al. The Earth's core as a reservoir of water. *Nat. Geosci.* **2020**, *13*, 453–458. https://doi.org/10.1038/s41561-020-0578-1.
17. Li, Y.G.; Vočadlo, L.; Ballentine, C.; et al. Primitive noble gases sampled from ocean island basalts cannot be from the Earth's core. *Nat. Commun.* **2022**, *13*, 3770. https://doi.org/10.1038/s41467-022-31588-7.

18. Huang, D.; Li, Y.; Khan, A.; et al. Thermoelastic Properties of Liquid Fe-rich Alloys Under Martian Core Conditions. *Geophys. Res. Lett.* **2023**, *50*, e2022GL102271. https://doi.org/10.1029/2022GL102271.
19. Yang, H.; Dou, P.X.; Xiao, T.T.; et al. The Geophysical Properties of FeH_x Phases Under Inner Core Conditions. *Geophys. Res. Lett.* **2023**, *50*, e2023GL104493. https://doi.org/10.1029/2023GL104493.
20. Dou, P.X.; Brodholt, J.; Vočadlo, L.; et al. Ab Initio Evaluation of Point Defects in Bridgmanite Under Lower Mantle Conditions. *J. Geophys. Res. Solid Earth* **2025**, *130*, e2025JB031147. https://doi.org/10.1029/2025JB031147.
21. Li, Y.G.; Li, C.H.; Zhou, Y.; et al. A deeper and hotter Martian core-mantle differentiation inferred from FeO partitioning. *Sci. Bull.* **2025**, *70*, 429–436. https://doi.org/10.1016/j.scib.2024.11.046.
22. Li, Y.G.; Guo, X.; Vočadlo, L.; et al. The effect of water on the outer core transport properties. *Phys. Earth Planet. Inter.* **2022**, *329*, 106907. https://doi.org/10.1016/j.pepi.2022.106907.
23. Huang, D.; Li, Y.; Murakami, M. Low Viscosity of Peridotite Liquid: Implications for Magma Ocean Dynamics. *Geophys. Res. Lett.* **2024**, *51*, e2023GL107608. https://doi.org/10.1029/2023GL107608.
24. Wang, H.H.; Li, Y.G.; Zhang, L.; et al. Dynamic bonding analysis of the water diffusion mechanism in silicate melts. *Phys. Rev. B* **2025**, *111*, 104206. https://doi.org/10.1103/PhysRevB.111.104206.
25. Huang, Y.H.; Li, Y.G.; Alfe, D.; et al. Ab Initio Study of the Conductivities of B2 FeSi Under Core-Mantle Boundary Conditions. *Geophys. Res. Lett.* **2025**, *52*, e2025GL115024. https://doi.org/10.1029/2025GL115024.
26. Jiang, D.Y.; Xie, L.C.; Wang, L.Q. Current application status of multi-scale simulation and machine learning in research on high-entropy alloys. *J. Mater. Res. Technol. JMRT* **2023**, *26*, 1341–1374. https://doi.org/10.1016/j.jmrt.2023.07.233.
27. Zhang, L.; Han, J.; Wang, H.; et al. Deep Potential Molecular Dynamics: A Scalable Model with the Accuracy of Quantum Mechanics. *Phys. Rev. Lett.* **2018**, *120*, 143001. https://doi.org/10.1103/PhysRevLett.120.143001.
28. Friederich, P.; Häse, F.; Proppe, J.; et al. Machine-learned potentials for next-generation matter simulations. *Nat. Mater.* **2021**, *20*, 750–761. https://doi.org/10.1038/s41563-020-0777-6.
29. Zhang, L.; Wang, H.; Car, R.; et al. Phase Diagram of a Deep Potential Water Model. *Phys. Rev. Lett.* **2021**, *126*, 236001. https://doi.org/10.1103/PhysRevLett.126.236001.
30. Behler, J. Neural network potential-energy surfaces in chemistry: A tool for large-scale simulations. *Phys. Chem. Chem. Phys.* **2011**, *13*, 17930–17955. https://doi.org/10.1039/c1cp21668f.
31. Behler, J.; Parrinello, M. Generalized neural-network representation of high-dimensional potential-energy surfaces. *Phys. Rev. Lett.* **2007**, *98*, 146401. https://doi.org/10.1103/PhysRevLett.98.146401.
32. Wang, D.; Wu, Z.; Deng, X. Thermal conductivity of Fe-bearing bridgmanite and post-perovskite: Implications for the heat flux from the core. *Earth Planet. Sci. Lett.* **2023**, *621*, 118368. https://doi.org/10.1016/j.epsl.2023.118368.
33. Li, Z.; Scandolo, S. Deep-learning interatomic potential for iron at extreme conditions. *Phys. Rev. B* **2024**, *109*, 184108. https://doi.org/10.1103/PhysRevB.109.184108.
34. Li, Z.; Scandolo, S. Elasticity and Viscosity of hcp Iron at Earth's Inner Core Conditions From Machine Learning-Based Large-Scale Atomistic Simulations. *Geophys. Res. Lett.* **2022**, *49*, e2022GL101161. https://doi.org/10.1029/2022GL101161.
35. Zhang, Z.G.; Csányi, G.; Alfè, D. Partitioning of sulfur between solid and liquid iron under Earth's core conditions: Constraints from atomistic simulations with machine learning potentials. *Geochim. Cosmochim. Acta* **2020**, *291*, 5–18. https://doi.org/10.1016/j.gca.2020.03.028.
36. Zhang, Z.; Wang, W.; Liu, J.; et al. Oxygen Driving Hydrogen Into the Inner Core: Implications for the Earth's Core Composition. *Geophys. Res. Lett.* **2025**, *52*, e2024GL110315. https://doi.org/10.1029/2024GL110315.
37. Wang, J.; Gao, H.; Han, Y.; et al. MAGUS: Machine learning and graph theory assisted universal structure searcher. *Natl. Sci. Rev.* **2023**, *10*, nwad128. https://doi.org/10.1093/nsr/nwad128.
38. Zhang, Y.-W.; Sorkin, V.; Aitken, Z.H.; et al. Roadmap for the development of machine learning-based interatomic potentials. *Model. Simul. Mater. Sci. Eng.* **2025**, *33*, 023301. https://doi.org/10.1088/1361-651X/ad9d63.
39. Bartók, A.P.; Payne, M.C.; Kondor, R.; et al. Gaussian Approximation Potentials: The Accuracy of Quantum Mechanics, without the Electrons. *Phys. Rev. Lett.* **2010**, *104*, 136403. https://doi.org/10.1103/PhysRevLett.104.136403.
40. Unke, O.T.; Meuwly, M. PhysNet: A Neural Network for Predicting Energies, Forces, Dipole Moments, and Partial Charges. *J. Chem. Theory Comput.* **2019**, *15*, 3678–3693. https://doi.org/10.1021/acs.jctc.9b00181.
41. Zhang, Y.; Wang, H.; Chen, W.; et al. DP-GEN: A concurrent learning platform for the generation of reliable deep learning based potential energy models. *Comput. Phys. Commun.* **2020**, *253*, 107206. https://doi.org/10.1016/j.cpc.2020.107206.
42. Deng, J.; Niu, H.; Hu, J.; et al. Melting of $MgSiO_3$ determined by machine learning potentials. *Phys. Rev. B* **2023**, *107*, 064103. https://doi.org/10.1103/PhysRevB.107.064103.
43. Zeni, C.; Pinsler, R.; Zügner, D.; et al. A generative model for inorganic materials design. *Nature* **2025**, *639*, 624–632. https://doi.org/10.1038/s41586-025-08628-5.
44. Deng, B.W.; Zhong, P.C.; Jun, K.; et al. CHGNet as a pretrained universal neural network potential for charge-informed atomistic modelling. *Nat. Mach. Intell.* **2023**, *5*, 1031–1041. https://doi.org/10.1038/s42256-023-00716-3.

45. Chen, C.; Ong, S.P. A universal graph deep learning interatomic potential for the periodic table. *Nat. Comput. Sci.* **2022**, *2*, 718–728. https://doi.org/10.1038/s43588-022-00349-3.
46. Riebesell, J.; Goodall, R.E.A.; Benner, P.; et al. A framework to evaluate machine learning crystal stability predictions. *Nat. Mach. Intell.* **2025**, *7*, 836–847. https://doi.org/10.1038/s42256-025-01055-1.
47. Shimizu, K.; Suhara, K.; Ikumo, M.; et al. Superconductivity in oxygen. *Nature* **1998**, *393*, 767–769. https://doi.org/10.1038/31656.
48. Ma, Y.M.; Eremets, M.; Oganov, A.R.; et al. Transparent dense sodium. *Nature* **2009**, *458*, 182–185. https://doi.org/10.1038/nature07786.
49. Park, I.; He, Y.; Mao, H.K.; et al. Electride Formation of HCP-Iron at High Pressure: Unraveling the Origin of the Superionic State of Iron-Rich Compounds in Rocky Planets. *Adv. Sci.* **2024**, *11*, 2308177. https://doi.org/10.1002/advs.202308177.
50. Zhang, Y.; Gao, C.; Liu, Q.; et al. Warm dense matter simulation via electron temperature dependent deep potential molecular dynamics. *Phys. Plasmas* **2020**, *27*, 122704. https://doi.org/10.1063/5.0023265.
51. Yuan, L.; Steinle-Neumann, G. Hydrogen distribution between the Earth's inner and outer core. *Earth Planet. Sci. Lett.* **2023**, *609*, 118084. https://doi.org/10.1016/j.epsl.2023.118084.
52. Wu, F.; Wu, S.; Wang, C.-Z.; et al. Melting temperature of iron under the Earth's inner core condition from deep machine learning. *Geosci. Front.* **2024**, *15*, 101925. https://doi.org/10.1016/j.gsf.2024.101925.
53. Li, Y.G.; Ni, H.W. MD2D: A python module for accurate determination of diffusion coefficient from molecular dynamics. *Comput. Phys. Commun.* **2023**, *284*, 108599. https://doi.org/10.1016/j.cpc.2022.108599.
54. Eriksson, R.; Seetharaman, S. Thermal diffusivity measurements of some synthetic $CaO\text{-}Al_2O_3\text{-}SiO_2$ slags. *Metall. Mater. Trans. B Proc. Metall. Mater. Proc. Sci.* **2004**, *35*, 461–469. https://doi.org/10.1007/s11663-004-0047-z.
55. Hasegawa, H.; Hoshino, Y.; Kasamoto, T.; et al. Thermal Conductivity Measurements of Some Synthetic $Al_2O_3\text{-}CaO\text{-}SiO_2$ Slags by Means of a Front-Heating and Front-Detection Laser-Flash Method. *Metall. Mater. Trans. B Proc. Metall. Mater. Proc. Sci.* **2012**, *43*, 1405–1412. https://doi.org/10.1007/s11663-012-9702-y.
56. Kang, Y.; Morita, K. Thermal conductivity of the $CaO\text{-}Al_2O_3\text{-}SiO_2$ system. *ISIJ Int.* **2006**, *46*, 420–426. https://doi.org/10.2355/isijinternational.46.420.
57. Susa, M.; Watanabe, M.; Ozawa, S.; et al. Thermal conductivity of $CaO\text{-}SiO_2\text{-}Al_2O_3$ glassy slags:: Its dependence on molar ratios of Al_2O_3/CaO and SiO_2/Al_2O_3. *Ironmak. Steelmak.* **2007**, *34*, 124–130. https://doi.org/10.1179/174328107x165672.
58. Fei, H.Z.; Yamazaki, D.; Sakurai, M.; et al. A nearly water-saturated mantle transition zone inferred from mineral viscosity. *Sci. Adv.* **2017**, *3*, e1603024. https://doi.org/10.1126/sciadv.1603024.
59. Wang, D.; Wu, Z.; Deng, X. Thermal Conductivity of Hydrous Wadsleyite Determined by Non-Equilibrium Molecular Dynamics Based on Machine Learning. *Geophys. Res. Lett.* **2022**, *49*, e2022GL100337. https://doi.org/10.1029/2022GL100337.
60. Chang, Y.Y.; Hsieh, W.P.; Tan, E.; et al. Hydration-reduced lattice thermal conductivity of olivine in Earth's upper mantle. *Proc. Natl. Acad. Sci. USA* **2017**, *114*, 4078–4081. https://doi.org/10.1073/pnas.1616216114.
61. Marzotto, E.; Hsieh, W.P.; Ishii, T.; et al. Effect of Water on Lattice Thermal Conductivity of Ringwoodite and Its Implications for the Thermal Evolution of Descending Slabs. *Geophys. Res. Lett.* **2020**, *47*, e2020GL087607. https://doi.org/10.1029/2020GL087607.
62. Deng, J.; Stixrude, L. Thermal Conductivity of Silicate Liquid Determined by Machine Learning Potentials. *Geophys. Res. Lett.* **2021**, *48*, e2021GL093806. https://doi.org/10.1029/2021GL093806.
63. Peng, Y.; Deng, J. Thermal Conductivity of $MgSiO_3\text{-}H_2O$ System Determined by Machine Learning Potentials. *Geophys. Res. Lett.* **2024**, *51*, e2023GL107245. https://doi.org/10.1029/2023GL107245.
64. Deng, J. Large-Scale Atomistic Simulations of Magnesium Oxide Exsolution Driven by Machine Learning Potentials: Implications for the Early Geodynamo. *Geophys. Res. Lett.* **2024**, *51*, e2024GL109793. https://doi.org/10.1029/2024GL109793.
65. Luo, H.; Karki, B.B.; Ghosh, D.B.; et al. Anomalous Behavior of Viscosity and Electrical Conductivity of $MgSiO_3$ Melt at Mantle Conditions. *Geophys. Res. Lett.* **2021**, *48*, e2021GL093573. https://doi.org/10.1029/2021GL093573.
66. Peng, Y.; Deng, J. Hydrogen Diffusion in the Lower Mantle Revealed by Machine Learning Potentials. *J. Geophys. Res. Solid Earth* **2024**, *129*, e2023JB028333. https://doi.org/10.1029/2023JB028333.
67. Li, J.; Lin, Y.; Meier, T.; et al. Silica-water superstructure and one-dimensional superionic conduit in Earth's mantle. *Sci. Adv.* **2023**, *9*, eadh3784. https://doi.org/10.1126/sciadv.adh3784.
68. Reid, J.E.; Suzuki, A.; Funakoshi, K.I.; et al. The viscosity of $CaMgSi_2O_6$ liquid at pressures up to 13 GPa. *Phys. Earth Planet. Inter.* **2003**, *139*, 45–54. https://doi.org/10.1016/S0031-9201(03)00143-2.
69. Behrens, H.; Schulze, F. Pressure dependence of melt viscosity in the system $NaAlSi_3O_8\text{-}CaMgSi_2O_6$. *Am. Miner.* **2003**, *88*, 1351–1363. https://doi.org/10.2138/am-2003-8-919.
70. Suzuki, A.; Ohtani, E.; Terasaki, H.; et al. Viscosity of silicate melts in $CaMgSi_2O_6\text{-}NaAlSi_2O_6$ system at high pressure. *Phys. Chem. Miner.* **2005**, *32*, 140–145. https://doi.org/10.1007/s00269-005-0452-0.
71. Spice, H.; Sanloup, C.; Cochain, B.; et al. Viscosity of liquid fayalite up to 9 GPa. *Geochim. Cosmochim. Acta* **2015**, *148*, 219–227. https://doi.org/10.1016/j.gca.2014.09.022.

72. Liebske, C.; Schmickler, B.; Terasaki, H.; et al. Viscosity of peridotite liquid up to 13 GPa: Implications for magma ocean viscosities. *Earth Planet. Sci. Lett.* **2005**, *240*, 589–604. https://doi.org/10.1016/j.epsl.2005.10.004.
73. Cochain, B.; Sanloup, C.; Leroy, C.; et al. Viscosity of mafic magmas at high pressures. *Geophys. Res. Lett.* **2017**, *44*, 818–826. https://doi.org/10.1002/2016gl071600.
74. Luo, C.; Sun, Y.; Wentzcovitch, R.M. Probing the state of hydrogen in δ−AlOOH at mantle conditions with machine learning potential. *Phys. Rev. Res.* **2024**, *6*, 013292. https://doi.org/10.1103/PhysRevResearch.6.013292.
75. Peng, Y.; Yoshino, T.; Deng, J. Grain boundary diffusion cannot explain the W isotope heterogeneities of the deep mantle. *Nat. Commun.* **2025**, *16*, 1866. https://doi.org/10.1038/s41467-025-57120-1.
76. Li, Z.; Scandolo, S. Short-range order stabilizes a cubic iron alloy in Earth's inner core. *Nat. Commun.* **2025**, *16*, 7574. https://doi.org/10.1038/s41467-025-62666-1.
77. Zhang, Y.; Wang, W.; Li, Y.; et al. Superionic iron hydride shapes ultralow-velocity zones at Earth's core–mantle boundary. *Proc. Natl. Acad. Sci. USA* **2024**, *121*, e2406386121. https://doi.org/10.1073/pnas.2406386121.
78. Zhang, C.; Yang, J.-Y.; Sun, T.; et al. Strong precursor softening in cubic $CaSiO_3$ perovskite. *Proc. Natl. Acad. Sci. USA* **2025**, *122*, e2410910122. https://doi.org/10.1073/pnas.2410910122.
79. Knittle, E.; Jeanloz, R. Melting Curve of (Mg,Fe)SiO_3 Perovskite to 96 GPa—Evidence for a Structural Transition in Lower Mantle Melts. *Geophys. Res. Lett.* **1989**, *16*, 421–424. https://doi.org/10.1029/GL016i005p00421.
80. Heinz, D.L.; Jeanloz, R. Measurement of the Melting Curve of $Mg_{0.9}Fe_{0.1}SiO_3$ at Lower Mantle Conditions and Its Geophysical Implications. *J. Geophys. Res. Solid Earth and Planets* **1987**, *92*, 11437–11444. https://doi.org/10.1029/JB092iB11p11437.
81. Akins, J.A.; Luo, S.N.; Asimow, P.D.; et al. Shock-induced melting of $MgSiO_3$ perovskite and implications for melts in Earth's lowermost mantle. *Geophys. Res. Lett.* **2004**, *31*, L14612. https://doi.org/10.1029/2004gl020237.
82. Shen, G.Y.; Lazor, P. Measurement of Melting Temperatures of Some Minerals under Lower Mantle Pressures. *J. Geophys. Res. Solid Earth* **1995**, *100*, 17699–17713. https://doi.org/10.1029/95jb01864.
83. Ito, E.; Katsura, T. Melting of Ferromagnesian Silicates Under the Lower Mantle Conditions. In *High-Pressure Research: Application to Earth and Planetary Sciences*, 1st ed.; Syono, Y., Manghnani, M.H., Eds.; American Geophysical Union: Washington, DC, USA, 1992; pp. 315–322. https://doi.org/10.1029/GM067p0315.
84. Zerr, A.; Boehler, R. Melting of (Mg,Fe)SiO_3-perovskite to 625 Kilobars—Indication of a High-Melting Temperature in the Lower Mantle. *Science* **1993**, *262*, 553–555. https://doi.org/10.1126/science.262.5133.553.
85. Stixrude, L.; Karki, B. Structure and freezing of $MgSiO_3$ liquid in Earth's lower mantle. *Science* **2005**, *310*, 297–299. https://doi.org/10.1126/science.1116952.
86. Di Paola, C.; Brodholt, J.P. Modeling the melting of multicomponent systems: The case of $MgSiO_3$ perovskite under lower mantle conditions. *Sci. Rep.* **2016**, *6*, 29830. https://doi.org/10.1038/srep29830.
87. Liu, Z.J.; Zhang, C.R.; Sun, X.W.; et al. The melting curve of $MgSiO_3$ perovskite from molecular dynamics simulation. *Phys. Scr.* **2011**, *83*, 045602. https://doi.org/10.1088/0031-8949/83/04/045602.
88. Belonoshko, A.B.; Skorodumova, N.V.; Rosengren, A.; et al. High-pressure melting of $MgSiO_3$. *Phys. Rev. Lett.* **2005**, *94*, 195701. https://doi.org/10.1103/PhysRevLett.94.195701.
89. Hirose, K.; Sinmyo, R.; Sata, N.; et al. Determination of post-perovskite phase transition boundary in $MgSiO_3$ using Au and MgO pressure standards. *Geophys. Res. Lett.* **2006**, *33*, L01310. https://doi.org/10.1029/2005gl024468.
90. Tateno, S.; Hirose, K.; Sata, N.; et al. Determination of post-perovskite phase transition boundary up to 4400 K and implications for thermal structure in D″ layer. *Earth Planet. Sci. Lett.* **2009**, *277*, 130–136. https://doi.org/10.1016/j.epsl.2008.10.004.
91. Wang, Z.; He, Y.; Mao, H.-K.; et al. Superionicity of oxygen-deficient davemaoite and its impact on the deep-Earth oxidation cycle. *Sci. Adv.* **2025**, *11*, eadu8401. https://doi.org/10.1126/sciadv.adu8401.
92. Wu, F.; Sun, Y.; Wan, T.; et al. Deep-Learning-Based Prediction of the Tetragonal → Cubic Transition in Davemaoite. *Geophys. Res. Lett.* **2024**, *51*, e2023GL108012. https://doi.org/10.1029/2023GL108012.
93. Shakya, A.; Ghosh, D.B.; Jackson, C.; et al. Insights into core-mantle differentiation from bulk Earth melt simulations. *Sci. Rep.* **2024**, *14*, 18739. https://doi.org/10.1038/s41598-024-69873-8.
94. Luo, H.; Karki, B.B.; Ghosh, D.B.; et al. Deep neural network potentials for diffusional lithium isotope fractionation in silicate melts. *Geochim. Cosmochim. Acta* **2021**, *303*, 38–50. https://doi.org/10.1016/j.gca.2021.03.031.
95. Luo, H.; Karki, B.B.; Ghosh, D.B.; et al. Diffusional fractionation of helium isotopes in silicate melts. *Geochem. Perspect. Lett.* **2021**, *19*, 19–22. https://doi.org/10.7185/geochemlet.2128.